# Hot compression mechanism and comparative study on constitutive models of Mo-3vol.%$Al_2O_3$ alloys

Liying Yao[1, 2], Yimin Gao[1], Liujie Xu[3]

(1. State Key Laboratory for Mechanical Behavior of Materials, School of Materials Science and Engineering, Xi'an Jiaotong University, Xi'an 710049, China; 2. Graduate student, Department of Materials Science and Engineering, Hokkaido University, Kita13 Nishi 8, Kita-ku, Sapporo 060-8628, Japan 3. Henan Key Laboratory of High-temperature Structural and Functional Materials, Luoyang 471003, China)

## *Abstract:*

The hot compression tests for Mo-3vol.%$Al_2O_3$ alloys were conducted on a Gleeble-1500D thermo-mechanical simulator in the temperatures range of 1000-1300 °C and strain rates range of 0.005-1 $s^{-1}$. The hot deformation behavior, mechanism associated with microstructure evolution of Mo-3vol.%$Al_2O_3$ alloys was investigated by electron backscattering diffraction (EBSD) analysis. Three types of stress-strain curves were analyzed by quantifying the work hardening rate. The deformation mechanism at 1000-1300 °C mainly included the plastic deformation of Mo-3vol.%$Al_2O_3$ alloy, as well as the dynamic recovery and recrystallization of Mo matrix. The modified Arrhenius, Modified Johnson-Cook (JC) and modified Zerilli-Armstrong constitutive equations were established and evaluated by the correlation coefficient ($R_c$) and average absolute relative error ($\bar{\varepsilon}$). The flow stress of Mo-3vol.%$Al_2O_3$ alloys could be well predicted by those three constitutive models, but modified Arrhenius constitutive model had a higher predicated accuracy.

***Keywords***: Mo-3vol.%$Al_2O_3$ alloy, Hot compression deformation, Deformation mechanism, Constitutive model.

## *1. Introduction*

Molybdenum (Mo) and its alloys are highly promising candidates for high-temperature materials used as piercing plug for seamless tube manufacturing, hot-runner nozzles for missile, cutting wire for machining process and electrode for glass melting [1-3], due to their attractive properties, including high melting point of 2623 °C, good high-temperature strength, high-temperature creep resistance and corrosion resistance [4]. The addition of in-situ α-$Al_2O_3$ has been reported to greatly improve the strength and wear resistance of Mo alloys by refining the grains [5-7]. Xu et al. [5] prepared Mo alloy with ~10vol.% $Al_2O_3$ using liquid-solid method, and found the micro-sized $Al_2O_3$ can significantly increase wear resistance of Mo alloy. Zhou et al. [7] found that the room temperature compression strength of Mo/$Al_2O_3$ composites remarkably increased with increasing $Al_2O_3$ volume fraction, to 1150 MPa at 40 vol% $Al_2O_3$, nearly 1.67 times greater than that of pure Mo, accompanying with an increase in high-temperature compression strength at 1100 ℃ from 330 MPa to 550 MPa. With superior mechanical properties, Mo-$Al_2O_3$ alloy is considered as an idea material in the elevated temperature engineering applications, partly replacing powder metallurgy pure Mo. However, Mo-$Al_2O_3$ alloy possess inadequate ductility and poor hot workability [8], owing to the limited slide systems in Mo matrix with body-centered cubic (bcc) crystal structure and the dispersed brittle α-$Al_2O_3$ particles, especially when inhomogeneous and coarse α-$Al_2O_3$ particles locate at grain boundaries [9]. In addition, hot deformation process, like rolling or swaging, is essential for final Mo products to obtain fine-grained microstructure and excellent properties. Thus it is necessary to study the elevated temperature behavior of the α-$Al_2O_3$ particles reinforced Mo matrix composite under a compressive load.

Recently the majority of researches focused on the hot deformation process of pure Mo and Mo alloys, including the strain rate and temperature dependence of flow behavior and micro-structural evolution [8, 10], hot deformation strengthening mechanism of pure Mo in terms of strain hardening index and strain-rate sensitivity

exponent [8, 11], and their Arrhenius-type constitutive equations [11-13]. There is less research about the hot deformation behavior of Mo-$Al_2O_3$ alloys and corresponding deformation mechanism. Furthermore, the accuracy of constitutive equations describing the flow stress of metallic materials constructed by experimental hot deformation tests are important for numerical simulation process, which correctly formulate the technological parameters and improve the product quality [15]. Arrhenius constitutive equations and the dynamic recrystallization (DRX) activation energy of pure Mo were established at 900-1450 °C and 0.01-10 $s^{-1}$ by Wang et al. [11] and at 993-1143 K and 0.0005-0.02 $s^{-1}$ by Meng et al. [12]. Except for the most widely applied Arrhenius model proposed by Sellars and McTegart [18], various constitutive models were proposed to accurately describe the flow stress over decades, including phenomenological-based, physical-based, and artificial neural network models [11, 12, 16-20]. The main phenomenological-based models also includes Johnson-Cook (JC) model [16]. Modified Zerilli-Armstrong (ZA) model based on dislocation thermal activation has advantages with a simple form and high accuracy in BCC crystal structure materials, such as austenitic stainless steel [19] and tungsten alloy [22].

In present work, the fraction of α-$Al_2O_3$ in Mo alloys was designed as 3 vol.%, lower than the minimum addition ~10 vol.% $Al_2O_3$ in literatures [5-7]. It focused on hot compression deformation behavior of Mo-3vol.%$Al_2O_3$ alloy at temperatures of 1000-1300 °C and strain rates range of 0.005-1 $s^{-1}$. The deformation mechanisms associated with the evaluation of the microstructure of the alloy was discussed. Moreover, the modified Arrhenius, JC [16] and KHL and modified ZA constitutive equations of Mo-3vol.%$Al_2O_3$ alloy were established and their prediction accuracy was evaluated.

## *2. Material and Experimental procedures*

The Mo-3vol.% $Al_2O_3$ alloys were prepared by solid-liquid (S-L) mixing powder metallurgy method. The AR commercial $(NH_4)_2Mo_4O_{13}\cdot 2H_2O$ and $Al(NO_3)_3\cdot 6H_2O$ were used as precursors. Firstly, $(NH_4)_2Mo_4O_{13}\cdot 2H_2O$ powders were heated at 520 °C for 4 h in a muffle furnace to prepare $MoO_3$ powders. Then $MoO_3$ powders were mixed

with the solution of $Al(NO_3)_3 \cdot 6H_2O$ by ball milling. The distilled water and ethanol were used as milling media. Next, the mixture was completely dried in drying cabinet at 90 °C. Finally, the mixed powders were reduced in a tube furnace with flowing hydrogen atmosphere, dwelling at 520 ℃ and 920 ℃ for 4h, respectively, to produce $Mo/Al_2O_3$ composite powders. The $Mo/Al_2O_3$ composite powders were filled into a cylinder rubber mold and pressed in cold isostatic press at 280 MPa for 20 min. After that, the pressed compact was sintered at 1920 °C for 3h in an intermediate frequency induction sintering furnace to prepare a rod with diameter of 20 mm. Multistep rotary swaging and surface polishing were carried out, machining it to a rod with diameter of 8 mm.

The hot compression testing specimens with the dimensions of Φ 8×12 mm were machined by WEDM (wire electrical discharge machining) and grinder. Then, a hole with Φ 0.1×1 mm was drilled for inserting the thermocouple. Fig. 1 shows the detailed schematic illustration of hot compression testing. The hot compression tests were conducted on a Gleeble-1500D thermo-mechanical simulator under four temperatures (1000 , 1100, 1200 and 1300 °C) and three strain rates (0.005, 0.1 and 1 $s^{-1}$), with true strain of 0.5. The compression samples were heated with the speed of 20 °C/s, and dwelled at target temperature for 3 min to ensure its homogeneous temperature distribution. The samples were water quenched immediately as soon as compression testing was completed. The true stress-strain curves were recorded automatically at different deformation conditions.

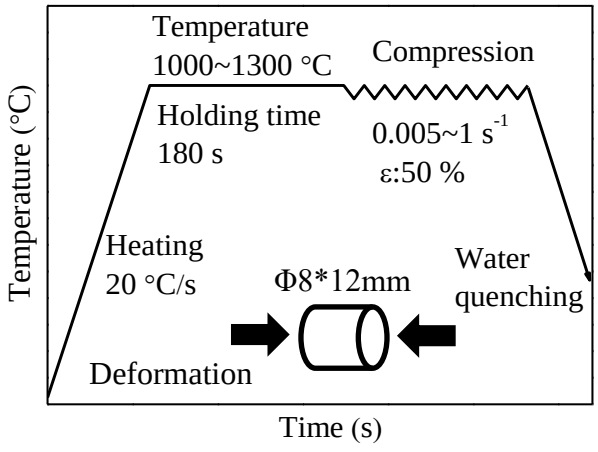


Fig.1. Schematic illustration of hot compression tests

For SEM and EBSD observation, samples with the thickness of 2 mm were cut from the middle parallel to the compression direction (CD) by WEDM. The section was ground using a series of SiC papers of varying grit sizes (e.g., 240, 400, 600, 800, 1000, 1200, 1500, 2000 grit) followed by mechanically polished with 3 and 0.1 μm alumina abrasive on a cloth pad for 20 minute. Finally, the chemcial-polishing with collodidal silica (OPS solution) was carried out to slightly etch the sample surface and remove the deformation layer during mechanical polishing. EBSD scanning with a step size of 0.1 μm was performed in a JSM-6500F (JEOL) FE-SEM scanning electron microscope operated at the accelerating voltage of 20 kV. The post analysis of the scanned data was carried out using the EDAX-OIM software.

## *3. Results and Discussion*

### *3.1 Flow curves analysis*

Fig. 2 shows the typical compressive ture stress-strain curves of Mo-3vol.%$Al_2O_3$ alloy. As with the thermally activated deformation of other metallic materials [13], the flow stress of Mo-3vol.%$Al_2O_3$ alloy decreased with increasing deformation temperature and decreasing strain rate. For example, the 0.2% flow stress at the strain rate of 1 $s^{-1}$ decreases from 378.99 MPa at 1000 ◦C to 347.09 MPa at 1300 ◦C, which is nearly 1.63 and 1.84 times as that of pure Mo at the same deformation condition (232.04 MPa and 188.21 MPa at 1000 and 1300 ◦C, respectively ). Raghunath et al. [23] pointed out that the migration and annihilation of dislocations are enhanced at high temperature. Thus metals get softer when heated. Moreover, low strain rate provides more time available to move boundaries, which result in lower flow stress.

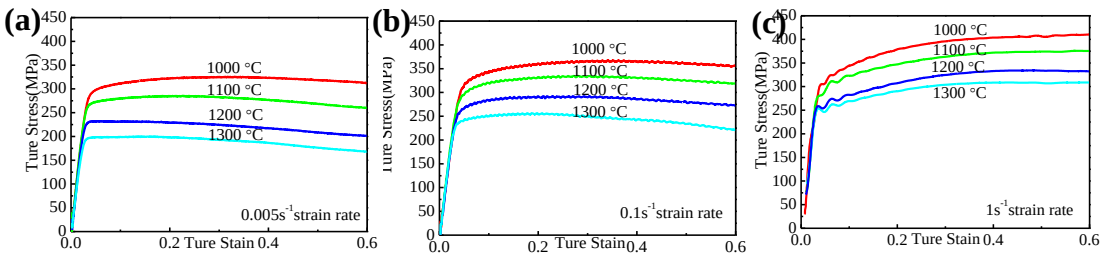

Fig.2. Ture stress- strain curves of Mo-3vol.%$Al_2O_3$ alloys in different temperature at strain rate of: (a) 0.005 $s^{-1}$, (b) 0.1 $s^{-1}$ and (c) 1 $s^{-1}$.

It also can be seen that three types of flow curves of Mo-3vol.%$Al_2O_3$ alloys are exhibited under investigated deformation conditions: (i) continuous increase in stress with strain (at temperature of 1100-1300 °C and strain rates of 1 $s^{-1}$ as shown in in Fig. 2 (c)); (ii) increase in stress with strain until steady stress is achieved (at temperature of 1100-1200 °C and strain rate of 0.1 $s^{-1}$ see in Fig. 2 (b)); (iii) increase in stress until peak stress achieves and then decrease with strain (at temperature of 1100-1300 °C and strain rate of 0.005 $s^{-1}$ see in Fig. 2 (a)). It is due to the competition between work hardening and dynamic softening. In order to quantify the effect of the combination of work hardening and dynamic softening on flow stress, the work hardening rate ($\theta=d\sigma/d\varepsilon$) was determined by the fitting and differentiation of true stress-strain curves and shown in Fig. 3. The value of work hardening rate depends on the competition between work hardening and dynamic softening, which is positive if work hardening dominates. At the beginning of plastic deformation, work hardening rate is extremely high because dislocations generate and hinder each other from moving or hinder by second particles, resulting in significantly increasing in flow stress. Subsequently, work hardening rate fall rapidly because dynamic recovery occurs firstly with partial dislocation annihilation to relief internal stress. Flow stress further increases until peak value is reached at the work hardening rate of 0. As the deformation continues, the dynamic recrystallization appears with the nucleation and growth of new grain via the migration of high angle boundaries at continued strain. Generally, the peak stress ($\sigma_p$) and peak strain ($\varepsilon_p$) are defined as the flow stress and strain when work hardening rate ($\theta$) reaches 0 at the first time, which are listed in Table 1. It is worthwhile to note that peak strain obviously decreases with increasing temperature or decreasing strain rate-to 0.06-0.08 at 1300 °C or 0.005 $s^{-1}$ (see Fig.4(a)). At elevated temperature, the diffusion of vacancies and the associated climb of dislocations are expected to be higher activated. Meanwhile the low strain rate provides more time for dislocation annihilation. In other words, dynamic softening is more easily accomplished at higher temperature and lower

strain rate. At last, work hardening rate hovers around 0 until the compression is finished.

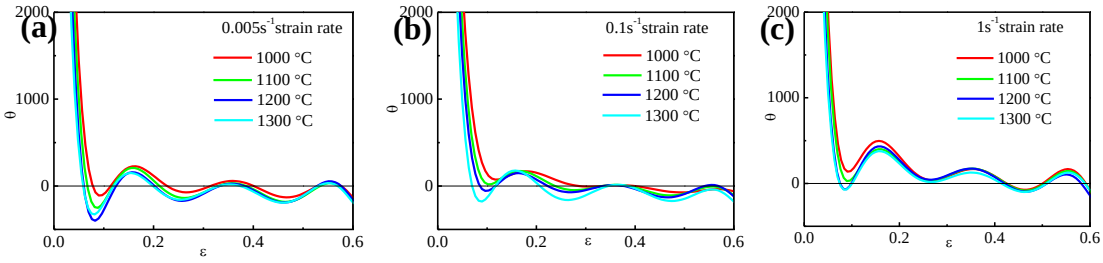


Fig.3. Strain hardening rate curves for Mo-3vol.%$Al_2O_3$ alloys in different temperature at strain rate of: (a) 0.005 $s^{-1}$, (b) 0.1 $s^{-1}$ and (c) 1 $s^{-1}$.

At 1100 °C/1 $s^{-1}$ and true strain of 0.5, the peak stress of Mo-3vol.%$Al_2O_3$ is about 45 MPa higher than that of Mo-10 vol.%$Al_2O_3$ prepared by Zhou et al. [7]. Fig.4(b) summarizes the peak compressive stress versus deformation temperature of several Mo alloys cited from literatures at the strain rate of 0.1 $s^{-1}$ and true strain of 0.5 [10, 27]. Mo-3vol.%$Al_2O_3$ alloy also highlights a high peak compressive stress among Mo alloys doped with different oxide types, about 110 MPa higher than that of pure Mo [10, 27], 50-80 MPa than that of 0.1-1.5 wt.% $ZrO_2$ dispersed strengthening Mo alloys [27] and . Al2O3 particles uniformly dispersed in Mo matrix, which contributes to the enhancement of 110 MPa by impedeing dislocation movement and refining Mo grain. In this work, the composite possess 3 vol.% $Al_2O_3$ particles, which is more than that of in the Mo-0.1-1.5 wt.% $ZrO_2$ (0.17-2.57 vol.%), showing a higher peak stress. In addition, with higher elestic modulus, $Al_2O_3$ particles (370 GPa) offer a more efficient strengening effect than $ZrO_2$ particles (233 GPa).

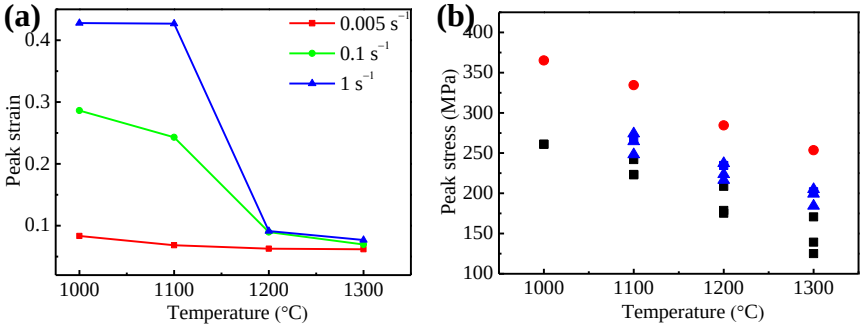

Fig.4. Effect of temperature on (a) peak strain of Mo-3vol.%$Al_2O_3$ alloy and (b) peak stress of several Mo alloys cited from literatures [10, 27] at strain rate of 0.1 $s^{-1}$and true strain of 0.5. Pure Mo (black filled square [10]), Mo-0.1-1.5 wt.%ZrO2 (Blue filled triangles, [27] ), Mo-3vol.%Al2O3(red filled circles, in present work)

Table 1 Measured peak stress and strain for Mo-3vol.%$Al_2O_3$ alloy under different deformation conditions

| | Peak stress (MPa) | | | Peak strain | | |
|---|---|---|---|---|---|---|
| | 0.005 $s^{-1}$ | 0.1 $s^{-1}$ | 1 $s^{-1}$ | 0.005 $s^{-1}$ | 0.1 $s^{-1}$ | 1 $s^{-1}$ |
| 1000 °C | 312.98 | 365.14 | 407.43 | 0.08 | 0.29 | 0.43 |
| 1100 °C | 284.76 | 334.43 | 375.37 | 0.07 | 0.24 | 0.43 |
| 1200 °C | 241.52 | 284.38 | 336.35 | 0.06 | 0.09 | 0.09 |
| 1300 °C | 206.82 | 253.53 | 267.88 | 0.06 | 0.07 | 0.08 |

### *3.2 High-temperature deformation Mechanism*

#### *3.2.1 plastic deformation of Mo-3vol.%$Al_2O_3$ alloy*

As shown in Fig.5, there exists two sizes of Al2O3 particles dispersing in Mo matrix—1-3 μm and several hundred nanometer respectively. Cracks perpendicular to the compression axis appears at Mo/micro-sized Al2O3 interface, while nano-sized Al2O3 particles do not cause cracks (see red arrow). Some potholes were left behind by the flaking of Al2O3 particles when polishing. At the elastic deformation stage of Mo-3vol.%Al2O3 alloy, stress concentration surrounds Al2O3 particles due to the huge elastic modulus difference between Al2O3 particle and ductile Mo matrix. When local stress exceeds the yield strength of Mo matrix, it begins to deform plastically, which releases dislocation and transforms stress to the Al2O3 particles at the same time. A great number of geometrically necessary dislocations would generate at Mo/Al2O3 interface. As the deformation continuous, the compatible deformation between Mo matrix and Al2O3 particles is further propelled by boundary slip or boundary fracture. Zhang [24] pointed out that it depends on the strength of Mo/Mo grain boundary and

the coherent strength of Mo/Al2O3 interface. The cracks of the Mo/micro Al2O3 interface illustrate there is a weaker cohesive strength between Mo matrix and micro Al2O3 than nano Al2O3 particles.

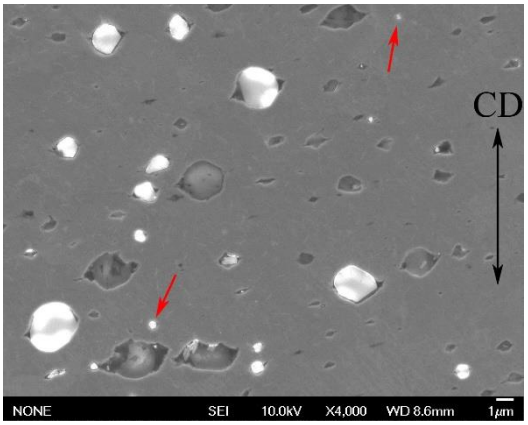


Fig.5. The Mo/Al2O3 interface cracks under a compressive stress at 1300 ◦C and 0.05$s^{-1}$ strain rate, CD: compression direction.

### *3.2.2 Dynamic recovery and recrystallization*

Fig.6 shows microstructure and misorientation angle of undeformed and deformed Mo-3vol.% Al2O3 alloy at 0.005 $s^{-1}$ strain rate and 1100-1300 ℃. Low angle grain boundaries (LAGBs) with misorientations of 2°-15° and high angle grain boundaries (HAGBs) with misorientations > 15° are delineated by green and black lines， respectively. The IQ map of initial Mo-3vol.%Al2O3 alloy before deformation shows the presentation of high fractions of HAGBs and fine grains. HAGBs accounts for 56.73 % and the mean misorientation is 23.78 %. A significant fraction of subgrains bounded by LAGBs in microstrure of deformed sample at 1100 ℃ and 0.005$s^{-1}$ is formed, with LAGBs fraction of 78.68 % and orientation difference of stress at 12.07 % (see in Fig.6 (c)). The fraction of LAGBs in deformed Mo-3vol.%Al2O3 alloy decreases to 77.58 % at 1200 ℃ and 66.37 % at 1300 ℃, while mean misorientation angle increases to 12.76 % and 15.69 %, separately. As the deformation begins, the metal lattice is elastically distorted, the dislocation density increases, and the dislocations are concentrated toward each other, resulting in dislocation climbing and cross-slip. Thus dynamic recovery competed with dislocation accumulation at the

beginning of deformation. When stored energy exceeds the critical amount of energy for formation of dynamic recrystallized grains, several neighborhooding subgrains combine to a new nuclea with HAGBs. In Fig.6 (c-h), the majority of GBs in deformed samples are LAGBs, because there is no enough time for subgrain to form recrystallized grains by mechanical rotation at high strain rate of 0.005 $s^{-1}$. The increase of average misorientation angle with temperature is related to the fraction of DRX nuclei.

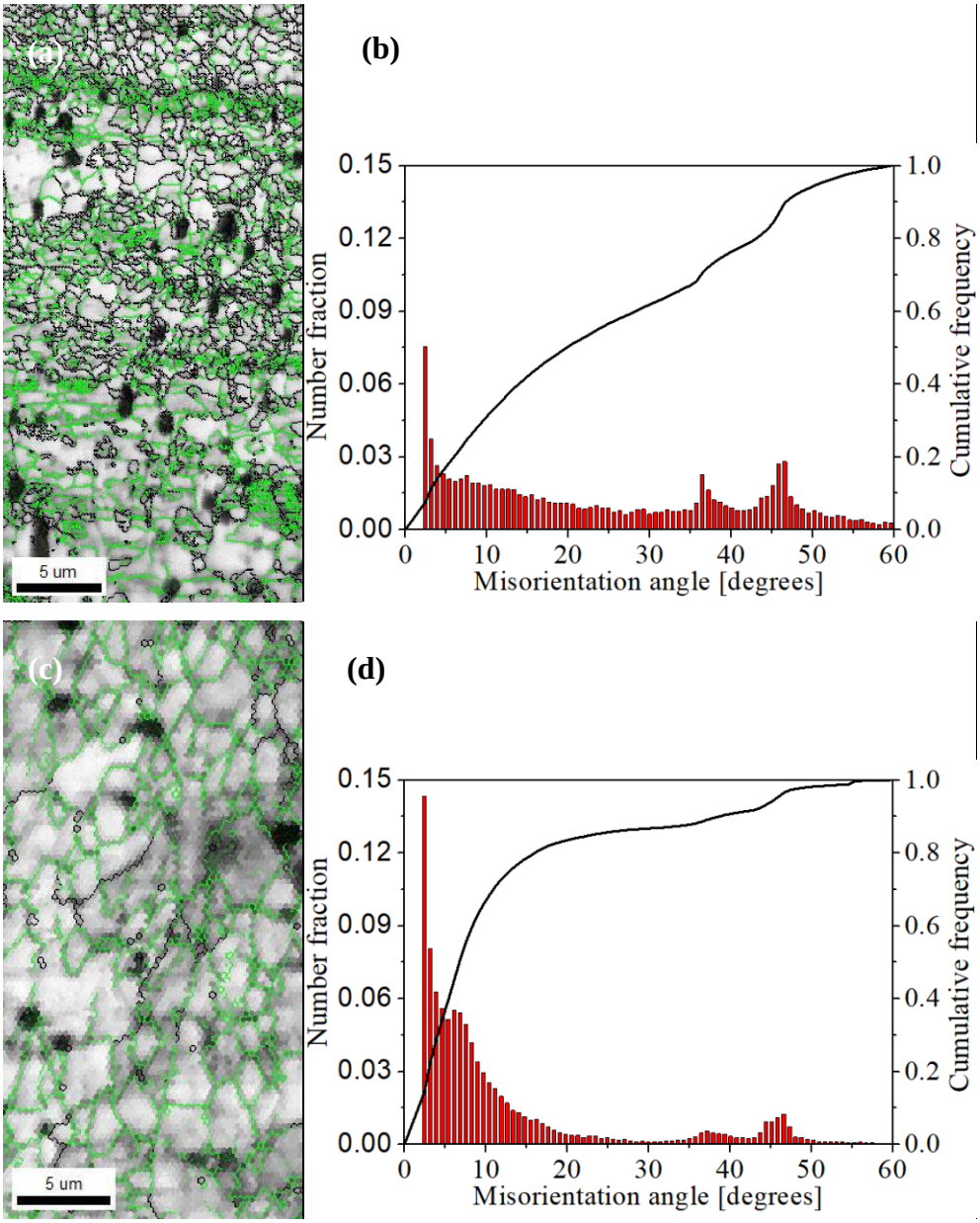

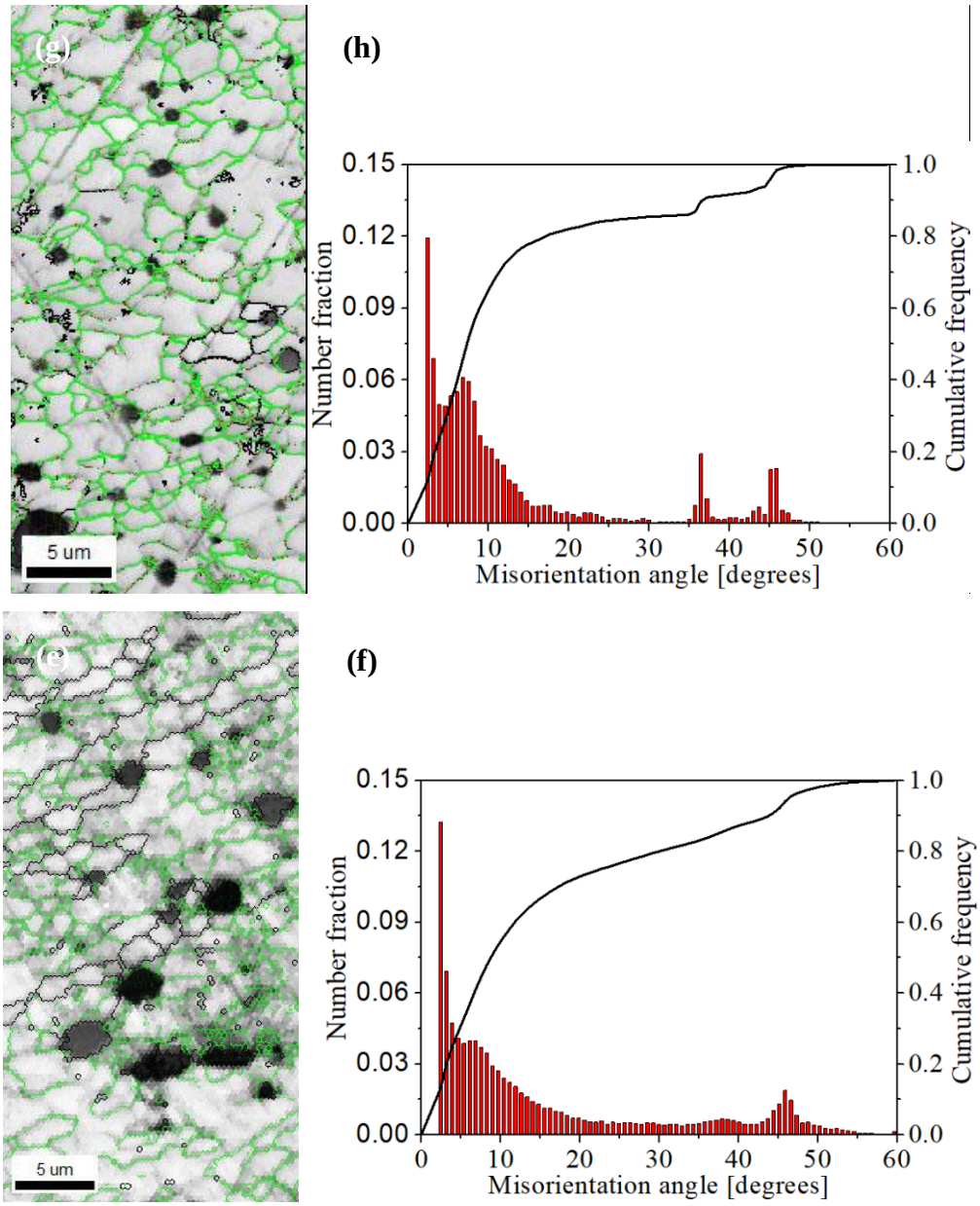


Fig.6. Microstructures and misorientation angle of (a)-(b) undeformed and deformed Mo-3vol.%$Al_2O_3$ alloy at 0.005 $s^{-1}$ at different deformation conditions: (c)-(d) 1100 ℃; (e)-(f) 1200 ℃; (g)-(h) 1300 ℃.

### *3.3 comparison of several constitutive model*

#### *3.3.1 Modified Arrhenius model*

Arrhenius model proposed by Sellars and McTegart [18] is generally applied to describe the relation among the deformation temperature, strain rate, stress and strain of metallic materials under different deformation conditions. The effects of deformation temperature and strain rate on the hot deformation behavior of metallic materials can

be represented by the Zener-Hollomon parameter (Z) in an exponent-type equation (see Eq. 2). The basic Arrhenius constitutive equations in hyperbolic sine form can be expressed as follows:

$$\dot{\varepsilon}=\begin{cases} A_1\sigma^{n_1}\exp\left(-\frac{Q}{RT}\right) & \alpha\sigma<0.8 \\ A_2\exp(\beta\sigma)\exp\left(-\frac{Q}{RT}\right) & \alpha\sigma>1.2 \\ A[\sinh(\alpha\sigma)]^n\exp\left(-\frac{Q}{RT}\right) & \text{for all } \sigma \end{cases} \quad (1)$$

$$Z=\dot{\varepsilon}\exp(Q/RT) \quad (2)$$

Where $\dot{\varepsilon}$ is the strain rate ($s^{-1}$), σ is the flow stress for a given strain (MPa), Q is the activation energy of hot deformation (kJ/mol), R is the universal gas constant (8.314 $J\bullet mol^{-1}\bullet K^{-1}$), T is the absolute temperature (K), $A_1(s^{-1})$, $A_2$, A, $n_1$, n, α ($MPa^{-1}$) are the materials constants ($\alpha=\beta/n_1$). Here, taking the flow stress at the ture strain of 0.6 as the σ term, the constants of constitutive equation for Mo-3vol.%$Al_2O_3$ alloys can be identified. Taking natural logarithms of both sides of Eq. (1):

$$\ln\dot{\varepsilon}=\begin{cases} n_1\ln\sigma+\ln A_1-\frac{Q}{RT} \\ \beta\sigma+\ln A_2-\frac{Q}{RT} \\ n[\sinh(\alpha\sigma)]+\ln A-\frac{Q}{RT} \end{cases} \quad (3)$$

The values of $n_1$ and β can be determined from the slope of the linear regression lines of lnε̇-lnσ and lnε̇-σ, which was derived from experimental true stress-true stain data (Fig. 3). As shown in Fig. 7, the mean value of $n_1$ and β are: $n_1$ = 13.2410, β = 0.0441. Thus, the calculated α value of Mo-3vol.%$Al_2O_3$ alloys at strain of 0.6 is 0.0033.

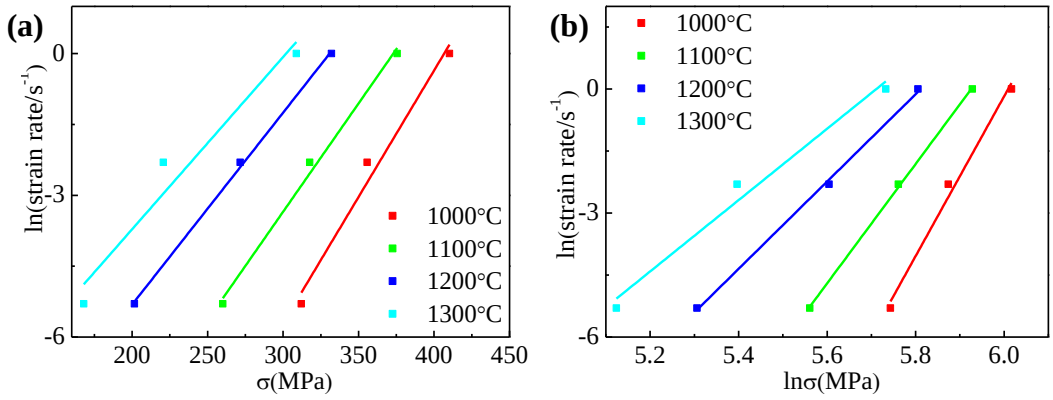


Fig.7. Relationships between: (a) ln ε̇ and ln σ; (b) ln ε̇ and σ.

Take partial derivation of 1/T of Eq. (3):

$$Q=R\left[\frac{\partial(\ln\dot{\varepsilon})}{\partial\ln[\sinh(\alpha\sigma)]}\right]_T R\left[\frac{\partial\ln[\sinh(\alpha\sigma)]}{\partial[1/T]}\right]_{\dot{\varepsilon}}=RnS \quad (4)$$

The values of n and S can be calculated from the slope of the linear regression lines of ln $\dot{\varepsilon}$-ln[sinh(ασ)] and ln[sinh(ασ)]-1000/T, as shown in Fig. 8. The mean value of n and S are: n=9.9579, S=3.9687. Thus, the activation energy Q for Mo-3vol.%$Al_2O_3$ alloys at strain of 0.6 can be determined as 321.4528 kJ/mol, which is lower than the self- diffusion activation energy of Mo (480 kJ/mol) [25].

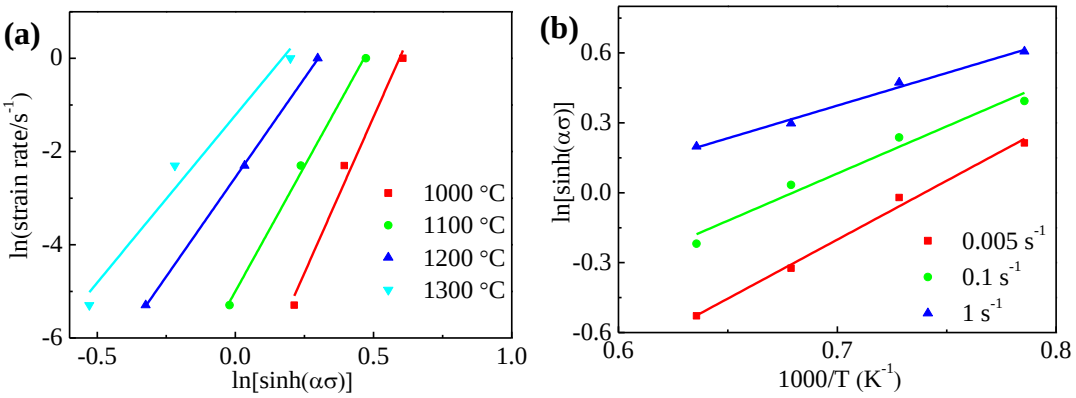


Fig.8. Relationships between: (a) ln[sinh(ασ)] and ln $\dot{\varepsilon}$; (b) ln[sinh(ασ)] and 1000/T.

Taking natural logarithms of both sides of Eq. (2):

$$\ln Z = n\ln[\sinh(\alpha\sigma)] + \ln A \quad (5)$$

As shown in Fig. 9, the values of lnA (24.3464) and n (9.3946) can be obtained from the relationship between ln[sinh(ασ)] and lnZ. Thus, the constitutive equation of Mo-3vol.%$Al_2O_3$ alloys at strain of 0.6 in the hyperbolic-sine function can be expressed as:

$$\dot{\varepsilon}=3.745\times10^{10}[\sinh(0.0033\sigma)]^{9.3946}\exp\left(-\frac{321.4528}{RT}\right) \quad (6)$$

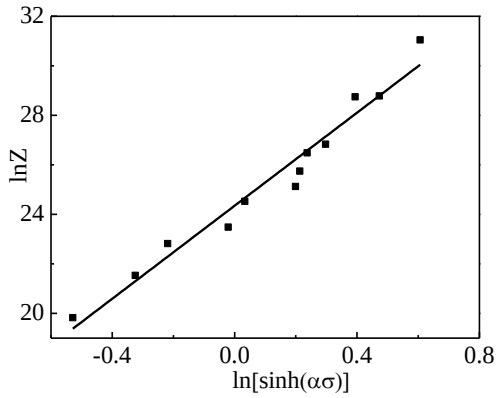


Fig.9. Relationship between lnZ and ln[sinh(ασ)].

In order to accurately predict the flow curves, Arrhenius constitutive equations were revised considering the strain effect during hot compression deformation. The constants of constitutive equation (α, Q, n , ln A) for Mo-3vol.%$Al_2O_3$ alloys were derivated by taking the flow stress in the strain range of 0.06-0.6 with an interval of 0.02. Variations of α, n, Q, ln A with true strain by 5th polynomial fit were shown in Fig. 8. The 5th polynomial fitting functions of the material constants were shown in Eq. (7) and the calculated coefficients of the polynomial were listed in Table 2.

$$\begin{cases} \alpha=B_0+B_1\varepsilon+B_2\varepsilon^2+B_3\varepsilon^3+B_4\varepsilon^4+B_5\varepsilon^5 \\ n=C_0+C_1\varepsilon+C_2\varepsilon^2+C_3\varepsilon^3+C_4\varepsilon^4+C_5\varepsilon^5 \\ Q=D_0+D_1\varepsilon+D_2\varepsilon^2+D_3\varepsilon^3+D_4\varepsilon^4+D_5\varepsilon^5 \\ \ln A=E_0+E_1\varepsilon+E_2\varepsilon^2+E_3\varepsilon^3+E_4\varepsilon^4+E_5\varepsilon^5 \end{cases} \quad (7)$$

Fig.10 shows the activation energy of hot deformation (Q), n and ln A value decreased with strain increased from 0.06 to 0.6, while the α values decreased firstly to $3.25954\times10^{-3}$ at the strain of 0.38 and then increased. Similar trend was showed in AZ31 magnesium alloys [27]. Meng et al. [12] established the Arrhenius constitutive equations of pure Mo and displayed the variations of α, n, Q and ln A with strain in strain range of 0.02-0.12 $s^{-1}$. An increase in Q, n and ln A with strain is in contradiction with the present observation. But these parameter has the same order of magnitude at the strain of 0.12.

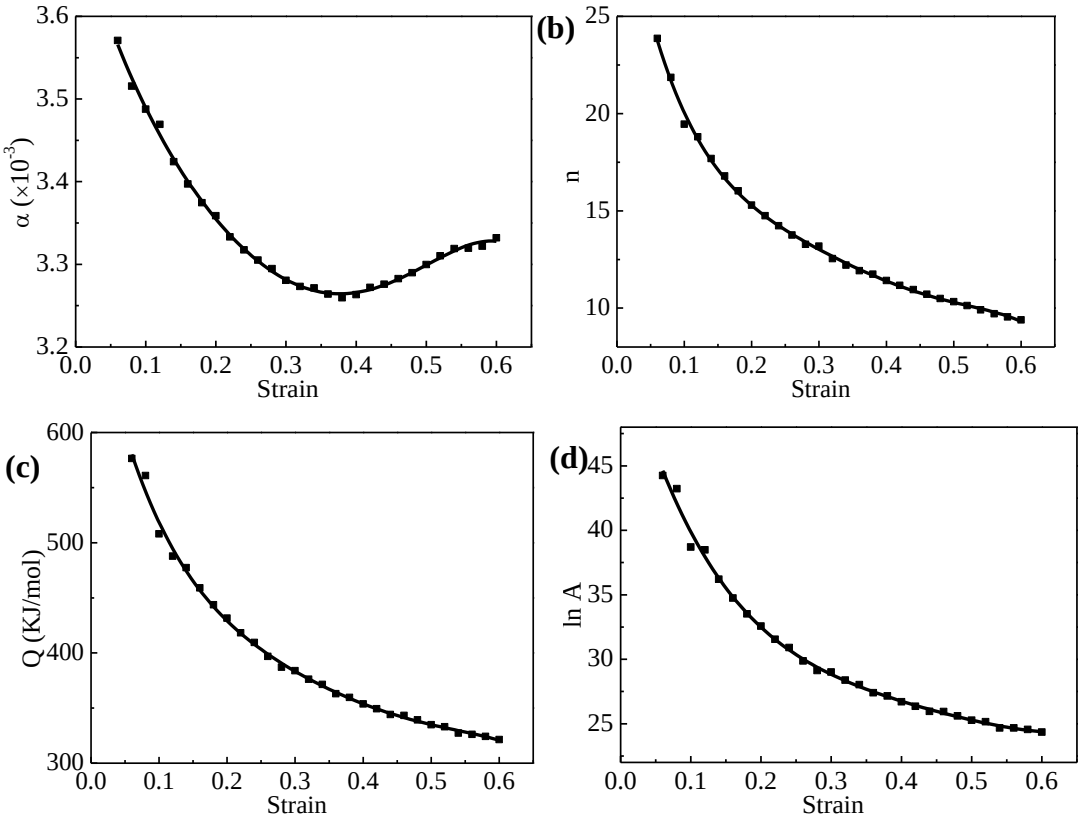


Fig.10. Variations of (a) α, (b) n, (c) Q, (d) ln A with true strain by 5th polynomial fit.

Thus, the modified Arrhenius constitutive equations based on expressing Z as a function of flow stress can be expressed as Eq. (8). The flow stresses under different deformation conditions can be calculated by combining Eq. (7) and Eq. (8).

$$\begin{cases} \sigma=\frac{1}{\alpha}\ln\left\{\left(\frac{Z}{A}\right)^{1/n}+\left[\left(\frac{Z}{A}\right)^{2/n}+1\right]^{1/2}\right\} \\ Z=\dot{\varepsilon}\exp\left(\frac{Q}{RT}\right) \end{cases} \tag{8}$$

Table 2 Coefficients of the polynomial for α, n, Q and ln A.

| α | n | Q | lnA |
|---|---|---|---|
| $B_0$= 3.7188 | $C_0$= 33.0101 | $D_0$= 721.4491 | $E_0$= 54.5805 |
| $B_1$=-3.03808 | $C_1$=-203.1505 | $D_1$=-2981.2862 | $E_1$=-199.4462 |
| $B_2$= 9.45918 | $C_2$= 954.2518 | $D_2$= 12046.0604 | $E_2$= 618.4668 |
| $B_3$=-24.4202 | $C_3$=-2500.8394 | $D_3$=-28679.3464 | $E_3$=-1017.5909 |
| $B_4$= 44.1832 | $C_4$= 3303.6365 | $D_4$= 35806.2767 | $E_4$= 787.1103 |

| | | | |
|---|---|---|---|
| $B_5$=-31.1827 | $C_5$=-1714.3332 | $D_5$=-17930.3160 | $E_5$=-197.9258 |

### *3.3.2 Modified Johnson-Cook (JC) model*

Johnson-Cook (JC) model is one of the widely used constitutive models because it has a few parameters and simple expression. However, this model considers the effects of temperature, strain rate and strain separately, which lead to a low accuracy. Therefore, a slight modification has been suggested in the original model which couples the effect of temperature, strain and strain rate. As shown in Eq. (9-10), The JC and the modified JC constitutive equations [16] can be expressed as:

$$\sigma = (A + B\varepsilon^{n})(1 + C\ln\dot{\varepsilon}^{*})(1 - T^{*m}) \quad (9)$$

$$\sigma = (A_1 + B_1\varepsilon + B_2\varepsilon^{2})(1 + C_1\ln\dot{\varepsilon})\exp[(\lambda_1 + \lambda_2\ln\dot{\varepsilon}^{*})(T - T_{ref})] \quad (10)$$

Where σ is the flow stress (MPa), A is the yield strength, B is a constant parameter of strain hardening, n is the strain hardening exponent, C is the strain rate intensity exponent, m is the thermo softening exponent, ε is the ture strain, $\dot{\varepsilon}$ is the strain rate ($s^{-1}$), $\dot{\varepsilon}^{*} = \dot{\varepsilon}/\dot{\varepsilon}_0$ is the dimensionless strain rate, where $\dot{\varepsilon}_0$ is the reference strain rate ($s^{-1}$), $T^{*} = \frac{T - T_{ref}}{T_m - T_{ref}}$, where, T, Tref and $T_m$ are the current and reference temperatures, the melting point (2896 K), respectively, $A_1$, $B_1$, $B_2$, $C_1$, $\lambda_1$ and $\lambda_2$ are the materials constants. The minimum temperature (1273K) and the maximum strain rate (1 $s^{-1}$) temperature are taken as the reference.

In this paper, L-M arithmetic (Levenberg-Marquardt) and UGO (Universal global optimization) fitting method in software 1stopt were used to fit the parameters of modified JC model, modified KHL model and modified ZA model. By fitting, the fitting values of parameters are listed in Table 3.

Table 3 Fitting results of parameters in the modified JC model

| $A_1$ | $B_2$ | $B_2$ | $C_1$ | $\lambda_1$ | $\lambda_2$ |
|---|---|---|---|---|---|
| 277.8013 | 691.1404 | -880.4234 | 0.0373 | -0.0009 | 0.0001 |

### *3.3.3 Modified Zerilli-Armstrong model*

Since the simple form and small calculation quantity, Zerilli-Armstrong (ZA) model is widely applied to describe the flow stress curves. However, this model does not consider the coupling effects of strain hardening, temperature softening and strain rate hardening on flow stress, which reduced the prediction accuracy. Therefore, modified ZA model were proposed by Samantaray et al. [19] to more accurately describe the hot deformation behavior of austenitic stainless steel by introducing an index variable ($c_1+c_2\varepsilon^n$). As shown in Eq. (12, 14), The ZA [19] and the modified ZA constitutive equations for molybdenum with body centered cubic (BCC) crystal structure can be expressed as:

$$\sigma = \sigma_0 + c_1\, exp(-c_3T + c_4Tln\dot{\varepsilon}) + c_5\varepsilon^n \quad (12)$$

$$\sigma=(c_1+c_2\varepsilon^n)\ \exp\left[-(c_3+c_4\varepsilon)T^*+(c_5+c_6T^*)ln\dot{\varepsilon}^*\right. \quad (13)$$

Where σ is the peak stress (MPa), $\sigma_0$ is the athermal part of yield strength and can be quantitatively given by $\Delta\sigma'_G+kD^{-1/2}$, where $\Delta\sigma'_G$ is the additional part of stress, k is the Hall-Petch constant (210MPa$\sqrt{\mu m}$), D is the average grain size. T is the absolute temperature (K), T*= T−Tref, where, T and Tref are the current and reference temperatures, respectively, ε is the ture strain, $\dot{\varepsilon}$ is the strain rate ($s^{-1}$), $\dot{\varepsilon}^* = \dot{\varepsilon}/\dot{\varepsilon}_0$ is the dimensionless strain rate, where, $\dot{\varepsilon}$ is the strain rate ($s^{-1}$) and $\dot{\varepsilon}_0$ is the reference strain rate ($s^{-1}$), the minimum temperature (1273K) and the maximum strain rate (1 $s^{-1}$) temperature are taken as the reference. $c_1$, $c_2$, $c_3$, $c_2$, $c_4$, $c_5$,$c_6$ and n are the materials constants. As shown in Table 5, the parameters of modified ZA model were listed by fitting in software 1stopt.

Table 5 Fitting results of parameters in the modified ZA model

| $c_1$ | $c_2$ | $c_3$ | $c_4$ | $c_5$ | $c_6$ | n |
|---|---|---|---|---|---|---|
| 464.4672 | -41.1988 | 0.0004 | 0.0015 | 0.0416 | 0.0001 | -0.4325 |

### *3.3.4 Predicting Accuracy*

In order to verify the predictability of three constitutive models, the predicted flow stress values were calculated by three constitutive models at different strain among 0.06-0.6 under different deformation conditions. Fig. 11 shows the comparisons between experimental flow stress values and predicted values from three constitutive equations. It can be seen that the predicted values were in accord with the experimental values. Previous research results have shown that modified Arrhenius model has relatively higher accuracy when deformation temperature and strain rate are varied greatly [21].

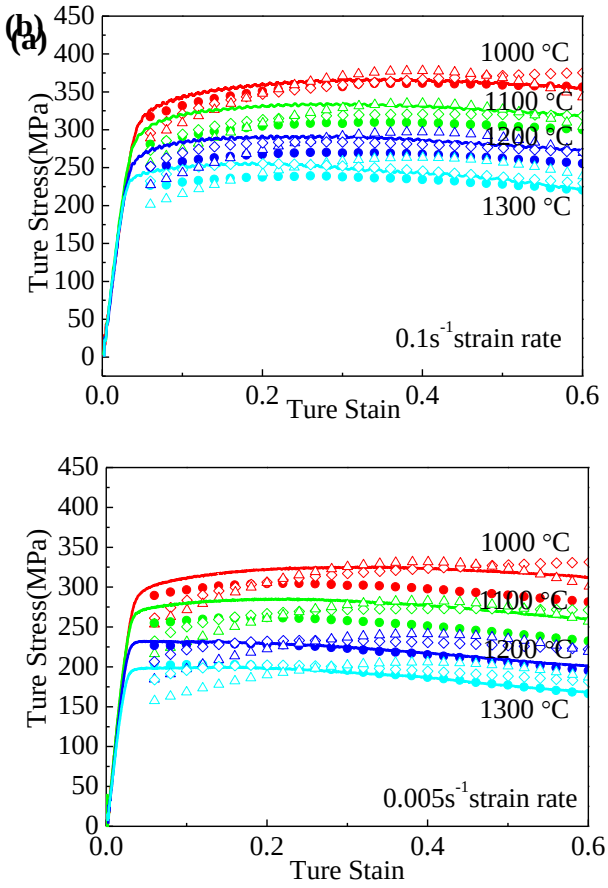

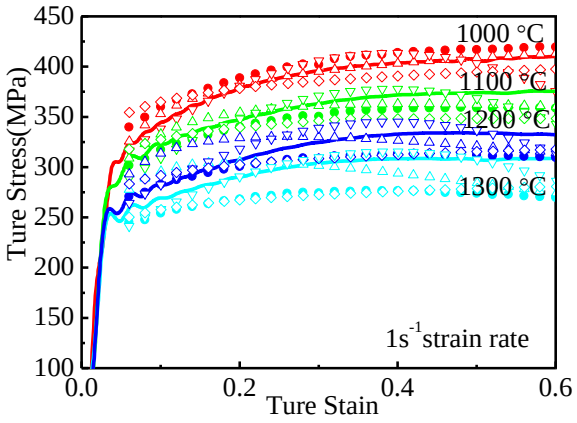


Fig.11. Comparisons between predicted value from modified Arrehnius (solid dots), modified JC (hollow upper triangle) and modified ZA (hollow diamond) equations and experimental flow stress (line) of Mo-3vol.%$Al_2O_3$ alloys at strain rate of: (a) 0.005 $s^{-1}$, (b) 0.1 $s^{-1}$ and (c) 1 $s^{-1}$.

**(c)**

In order to get the predication accuracy of three constitutive equations, the correlation coefficient ($R_c$) and average absolute relative error ($\bar{e}$) were introduced, which can be expressed as follows:

$$R_c=\frac{\sum_{i=1}^{N}(E_i-\bar{E})(P_i-\bar{P})}{\sqrt{\sum_{i=1}^{N}(E_i-\bar{E})(P_i-\bar{P})}} \tag{11}$$

$$\bar{e}=\frac{1}{N}\sum_{i=1}^{N}\left|\frac{E_i-P_i}{E_i}\right|\times 100\% \tag{12}$$

Where $E_i$ is the experimental flow stress, $P_i$ is the predicted flow stress, $\bar{E}$ is the average value of $E_i$, $\bar{P}$ is the average value of $P_i$, N is the number of evaluate data.

As shown in Fig. 12, the comparison of flow stress of modified Arrehnius model and modified ZA model. And the values of $R_c$ and $\bar{e}$ of two constitutive models were listed in Table.3. It can be seen that modified Arrehnius model has the highest correlation coefficient of 0.9918 and lowest average absolute relative error of 4.84 %. This indicated that modified Arrhenius model considering strain effect for Mo-3vol.%$Al_2O_3$ alloys has relatively higher predicated accuracy among three constitutive models.

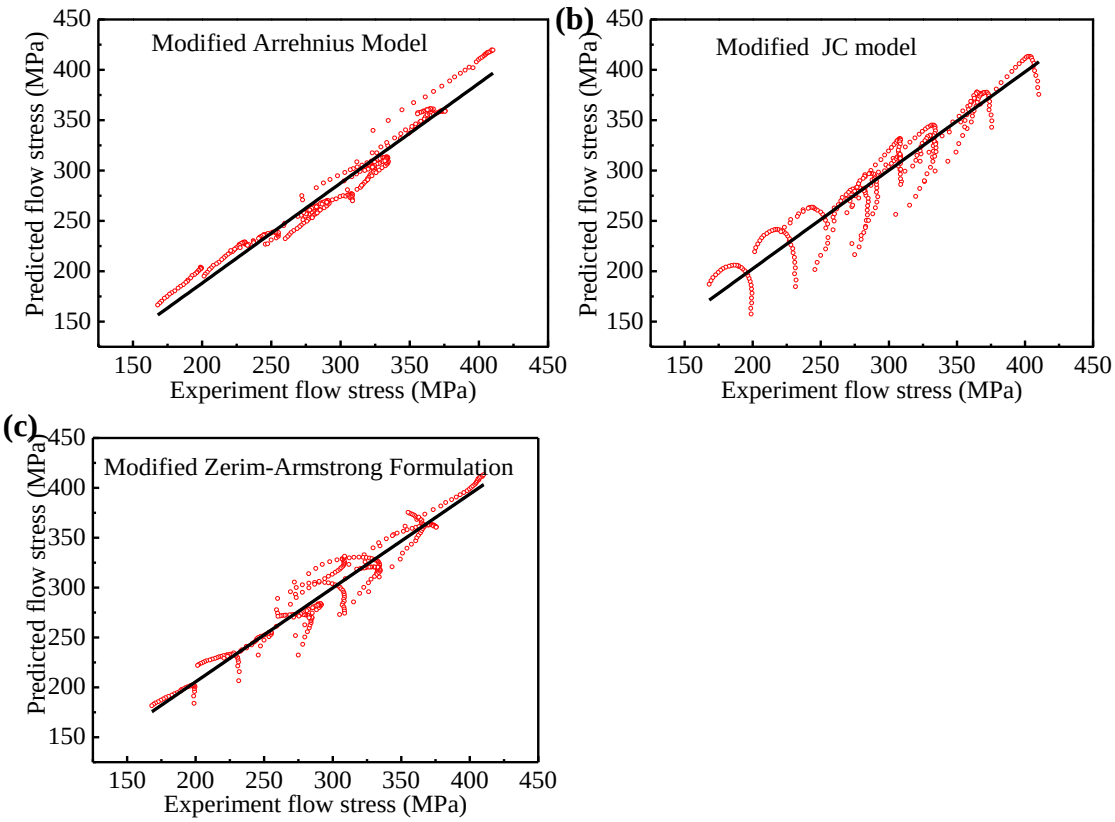


Fig.12. Comparison of flow stress calculated from (a) modified Arrehnius model, (b) modified JC model and (c) modified ZA model.

Table 6 Values of $R_c$ and $\bar{e}$ of two constitutive models

| | Modified Arrehnius model | Modified JC model | Modified ZA model. |
|---|---|---|---|
| Rc | 0.9918 | 0.9187 | 0.9726 |
| $\bar{e}$ | 4.84 | 4.87 | 10.11 |

## *5. Conclusions*

(1) Three types of stress-strain curves including work hardening, steady state and softening behavior were observed in Mo-3vol.% Al2O3 alloys depending upon the deformation condition and analysized by quantifying the work hardening rate.

(2) The deformation mechanism in the Mo-3vol.%Al2O3 alloy at 1000-1300 ℃ is responsible for the plastic deformation of Mo composite, as well as the dynamic recovery and recrystallization in the Mo matrix.

(3) The flow stress values predicted by the modified Arrhenius, modified JC and

modified ZA models agreed well with the experimental results. Compared their correlation coefficient (Rc) and average absolute relative error ($\bar{e}$), it is concluded that Arrhenius model considering strain effect predicated more accurately the flow stress of Mo-3vol.%$Al_2O_3$ alloys of 0.9918 and 4.84 among three constitutive models.

## *Acknowledgements*

This work was funded by the Key-Area Research and Development Program of GuangDong Province (2019B010942001), the Guangxi Innovation Driven Development Project (GUIKEAA18242001), the Fundamental Research Funds for the Central Universities of China (xzy012019001, xtr0118008).

## *References*

[1] G.-j. Zhang, G. Liu, Y.-j. Sun, F. Jiang, L. Wang, R. Wang and J. Sun, International Journal of Refractory Metals and Hard Materials 27, 173-176 (2009).

[2] J. H. Perepezko, Science 326, 1068-1069 (2009).

[3] X. Zhao and Z. Ye, Surface and Coatings Technology 228, S266-S270 (2013).

[4] S. Majumdar, S. Raveendra, I. Samajdar, P. Bhargava and I. Sharma, Acta materialia 57, 4158-4168 (2009).

[5] L. Xu, S. Wei, J. Li, G. Zhang and B. Dai, International Journal of Refractory Metals and Hard Materials 30, 208-212 (2012).

[6] L. Xu, S. Wei, D. Zhang, Y. Li, G. Zhang and J. Li, International Journal of Refractory Metals and Hard Materials 41, 483-488 (2013).

[7] Y. Zhou, Y. Gao, S. Wei, K. Pan and Y. Hu, International Journal of Refractory Metals and Hard Materials 54, 186-195 (2016).

[8] A. Chaudhuri, A. Sarkar and S. Suwas, International Journal of Refractory Metals & Hard Materials 73, 168-182 (2018).

[9] G. Liu, G. Zhang, F. Jiang, X. Ding, Y. Sun, J. Sun and E. Ma, Nature materials 12, 344-350 (2013).

[10] M. Xiao, F. Li, H. Xie and Y. Wang, Materials & Design 34, 112-119 (2012).

[11] Y. Wang, J. Peng, L. Zhong and F. Pan, Journal of Alloys and Compounds 681,

455-470 (2016).

[12] B. Meng, M. Wan, X. Wu, Y. Zhou and C. Chang, International Journal of Refractory Metals and Hard Materials 45, 41-47 (2014).

[13] A. Chaudhuri, A. N. Behera, A. Sarkar, R. Kapoor, R. K. Ray and S. Suwas, Acta Materialia 164, 153-164 (2019).

[14] E. Silva, H. Kestler and H. Sandim, International Journal of Refractory Metals and Hard Materials 73, 74-78 (2018).

[15] P. Follansbee and U. Kocks, Acta Metallurgica 36, 81-93 (1988).

[16] Y. Lin, L.-T. Li, Y.-X. Fu and Y.-Q. Jiang, Journal of Materials Science 47, 1306-1318 (2012).

[17] R.-x. Chai, C. Guo and L. Yu, *Materials Science and Engineering: A* **534**, 101-110 (2012).

[18] C. M. Sellars and W. McTegart, Acta Metallurgica 14, 1136-1138 (1966).

[19] D. Samantaray, S. Mandal, U. Borah, A. Bhaduri and P. Sivaprasad, Materials Science and Engineering: A 526, 1-6 (2009).

[20] F. J. Zerilli and R. W. Armstrong, Journal of applied physics 61, 1816-1825 (1987).

[21] R. Liang and A. S. Khan, International Journal of Plasticity 15, 963-980 (1999).

[22] J. Wang, G. Zhao, L. Chen and J. Li, Materials & Design 90, 91-100 (2016).

[23] S. Zhou, K. Deng, J. Li, K. Nie, F. Xu, H. Zhou and J. Fan, Materials & Design 64, 177-184 (2014).

[24] Y. Yan, L. Geng and A. Li, Materials Science and Engineering: A 448, 315-325 (2007).

[25] H. Johansen-Berg and T. E. Behrens, Diffusion MRI: from quantitative measurement to in vivo neuroanatomy, Academic Press(2013).

[26] Y. Wang, J. Peng, L. Zhong and F. Pan, Journal of Alloys and Compounds 681, 455-470 (2016).

[27] C. Cui, Y. Gao, S. Wei, G. Zhang, Y. Zhou and X. Zhu, Journal of Alloys and Compounds 716, 321-329 (2017).